

COMPLETE INFRARED SPECTRAL ENERGY DISTRIBUTIONS OF MM DETECTED QUASARS AT $Z > 5$

C. LEIPSKI¹, K. MEISENHEIMER¹, F. WALTER¹, M.-A. BESEL¹, H. DANNERBAUER², X. FAN³, M. HAAS⁴, U. KLAAS¹, O. KRAUSE¹, AND H.-W. RIX¹

Draft version August 20, 2018

ABSTRACT

We present *Herschel* far-infrared (FIR) photometry of eleven quasars at redshift $z > 5$ that have previously been detected at 1.2 mm. We perform full spectral energy distribution (SED) fits over the wavelength range $\lambda_{\text{rest}} \sim 0.1\text{--}400 \mu\text{m}$ for those objects with good *Herschel* detections. These fits reveal the need for an additional far-infrared (FIR) component besides the emission from a dusty AGN-powered torus. This additional FIR component has temperatures of $T_{\text{FIR}} \sim 40\text{--}60 \text{ K}$ with luminosities of $L_{8\text{--}1000\mu\text{m}} \sim 10^{13} L_{\odot}$ (accounting for 25–60% of the bolometric FIR luminosity). If the FIR dust emission is due to star formation it would suggest star formation rates in excess of 1000 solar masses per year. We show that at long wavelengths ($\lambda_{\text{rest}} \gtrsim 50 \mu\text{m}$) the contribution of the AGN-powered torus emission is negligible. This explains how previous FIR studies of high-redshift quasars that relied on single component fits to (ground-based) observations at $\lambda_{\text{obs}} \gtrsim 350 \mu\text{m}$ reached T_{FIR} and L_{FIR} values similar to our complete SED fits. Stacking the *Herschel* data of four individually undetected sources reveals a significant average signal in the PACS bands but not in SPIRE. The average SED of sources with individual *Herschel* detections shows a striking surplus in near- and mid-infrared emission when compared to common AGN templates. The comparison between two average SEDs (sources with and without individual *Herschel* detections) matched in the UV/optical indicates that for these objects the strength of the MIR emission may correlate with the strength of the FIR emission.

Keywords: Galaxies: active – quasars: general – Infrared: galaxies

1. INTRODUCTION

The presence of dust seems to be a ubiquitous property of galaxies throughout the observable universe. Even the most distant quasars at $z \sim 6$ show evidence for copious amounts of dust (e.g. Bertoldi et al. 2003; Beelen et al. 2006; Wang et al. 2008a; Leipski et al. 2010b). This indicates rapid metal enrichment of the interstellar medium within the first billion years after the big bang. About 30% of the known luminous $z \sim 6$ quasars are detected in the mm continuum with many of them also detected in CO (e.g. Wang et al. 2008a, and references therein). Such studies confirm the notion that most of the rest-frame far-infrared (FIR) emission comes from massive star formation, possibly indicating the formation of early galactic bulges. Thus, these objects signify an important stage in the connection between the build-up of stellar mass and black hole growth.

Most high-redshift objects lack full FIR/sub-mm spectral energy distributions (SEDs). L_{FIR} and M_{dust} are commonly determined using single photometric measurements, typically obtained at 1.2 mm (= 250 GHz) and applying standard values for the dust temperature as determined from lower redshift objects. It is unknown whether this assumption is appropriate for high-redshift objects. Ground-based 350 μm observations of a few $z > 5$ quasars tentatively support the assumed values

for the dust temperatures when combined with further sub-mm and mm data (Wang et al. 2008b).

For a more comprehensive picture of the dust emission at high redshifts we have obtained PACS (100+160 μm) and SPIRE (250+350+500 μm) photometry of 69 quasars at $z > 5$ as part of our *Herschel*⁵ Space Observatory (Pilbratt et al. 2010) key project “The Dusty Young Universe”. *Spitzer* Space Telescope (Werner et al. 2004) observations complement these data. This enables the study of the full optical through infrared SED of these objects in the rest frame wavelength range 0.5 – 80 μm , which – most importantly – covers the FIR peak of the SED. While the photometry for the complete key project sample will be presented in a forthcoming paper, we here report on the *Herschel* observations and SED analysis of the eleven objects in the sample which were previously detected at 1.2 mm (Tab. 1). Currently, this sub-sample is best suited to explore the relative importance of FIR and sub-mm/mm measurements for the interpretation of the total infrared SED and the contribution from the coolest dust components. Moreover, the increased wavelength coverage allows us to develop our fitting procedure with optimal constraints.

We outline the data reduction in Section 2. In Section 3 we describe how we extract physical properties from our measurements, which are then discussed in Section 4. We summarize and conclude in Section 5. Throughout the paper we use a Λ CDM cosmology with $H_0 = 71 \text{ km s}^{-1} \text{ Mpc}^{-1}$, $\Omega_{\text{m}} = 0.27$, and $\Omega_{\Lambda} = 0.73$.

2. OBSERVATIONS AND DATA REDUCTION

⁵ *Herschel* is an ESA space observatory with science instruments provided by European-led Principal Investigator consortia and with important participation from NASA.

¹ Max-Planck Institut für Astronomie (MPIA), Königstuhl 17, D-69117 Heidelberg, Germany; email: leipski@mpia-hd.mpg.de

² Universität Wien, Institut für Astronomie, Türkenschanzstraße 17, 1080 Wien, Austria

³ Steward Observatory, University of Arizona, Tucson, AZ 85721, USA

⁴ Astronomisches Institut Ruhr-Universität Bochum, Universitätsstraße 150, D-44801 Bochum, Germany

Table 1
The sample.

name SDSS	redshift	m_{1450} mag	$f_{250\text{ GHz}}$ mJy	References
(1)	(2)	(3)	(4)	(5)
J020332.35+001228.6	5.72	20.94	1.85 ± 0.46	1 , 2
J033829.30+002156.2	5.03	20.01	3.7 ± 0.3	4 , 5
J075618.13+410408.5	5.11	20.15	5.5 ± 0.5	6 , 7
J081827.40+172251.8	6.00	19.34	1.19 ± 0.38	8 , 3
J084035.09+562419.9	5.84	20.04	3.20 ± 0.64	8 , 9
J092721.82+200123.7	5.77	19.87	4.98 ± 0.75	8 , 3
J104433.04-012502.2	5.78	19.21	1.82 ± 0.43	10 , 3
J104845.05+463718.3	6.23	19.25	3.0 ± 0.4	11 , 12
J114816.64+525150.2	6.42	19.03	5.0 ± 0.6	11 , 12
J133550.80+353315.8	5.90	19.89	2.34 ± 0.50	8 , 9
J205406.42-000514.8	6.04	20.60	2.38 ± 0.53	1 , 3

Note. — (1) SDSS name ordered by R.A.; (2) redshift confirmed by CO measurements or NIR spectroscopy where available (see Appendix); (3) Apparent AB magnitude at 1450 Å in the rest frame of the quasar, corrected for galactic extinction; (4) Observed 250 GHz flux in mJy. Errors are 1σ ; (5) References for columns (3) and (4), respectively.

References. — (1) Jiang et al. 2008; (2) Wang et al. 2011; (3) Wang et al. 2008a; (4) Fan et al. 1999; (5) Carilli et al. 2001; (6) Wang et al. 2008b; (7) Petric et al. 2003; (8) Fan et al. 2006; (9) Wang et al. 2007; (10) Fan et al. 2001; (11) Fan et al. 2003; (12) Bertoldi et al. 2003

2.1. PACS

All objects were observed with the Photodetector Array Camera and Spectrometer (PACS; Poglitsch et al. 2010) at 100 and 160 μm using the mini-scan map observing template. For each source we obtained two maps with different scan angles using observing parameters as recommended in the mini-scan map Astronomical Observation Template (AOT) release note⁶. For each scan direction, five repetitions were executed. This resulted in a total on-source integration time of ~ 900 s for each object.

Data reduction was performed within the Herschel Interactive Processing Environment (HIPE, Ott 2010), version 8.0.1. We followed standard procedures for deep field data reduction, including source masking and high-pass filtering. The maps of the two scan directions were processed individually and mosaicked at the end of the workflow. A first version of the combined map was used to create a source mask for high-pass filtering. Masking was performed by hand through visual inspection of the mosaicked maps. This proved to be more reliable than a strict sigma cut, as it also allowed the masking of faint structures which can potentially influence the fluxes of faint targets if located close to the object of interest. A second processing was then performed, including the mask. The resulting maps (individual and mosaic) were inspected visually and if necessary the mask or width of the high-pass filter was adjusted. Images around the target positions at 100 and 160 μm are presented in Fig. 1.

Aperture photometry of the final mosaics was performed in IDL. We used relatively small apertures of 6''-10'' radius to maximize the signal-to-noise ratio. Appropriate aperture corrections were determined from tabulated values of the Encircled Energy Fraction of unresolved sources. Details on the properties of the PACS Point Spread Function (PSF) can be found on the PACS calibration web pages⁷.

The uncertainty in the photometry of our maps cannot

be determined directly from the pixel-to-pixel variations because the final PACS maps suffer from correlated noise (where the level of pixel noise correlation depends on the details of the data reduction and final map projection). In order to estimate robust photometric uncertainties we therefore implemented the following procedure: For any given map a set of 500 apertures of the same size as used for the QSO photometry was placed on random positions on the sky (see also Lutz et al. 2011; Popesso et al. 2012). The only constraint on the placement of these background apertures was that the central pixel of the aperture has to have at least 75 % of the integration time as the position of the QSO (to exclude noisy areas at the edge of the map). The distribution of the measured fluxes in these 500 apertures was then fitted by a Gaussian. The sigma value of this Gaussian was taken as the 1σ photometric uncertainty of this map. The resulting flux values for the quasars are given in Table 2.

2.2. SPIRE

All quasars in the sample were also observed with the Spectral and Photometric Imaging Receiver (SPIRE, Griffin et al. 2010) at 250, 350, and 500 μm in small scan map mode for five repetitions and a total on-source integration time of ~ 190 s per source. Data reduction followed standard procedures in HIPE as recommended by the SPIRE instrument team. Source extraction was performed with the HIPE build-in task 'sourceExtractorSussextractor' (Savage & Oliver 2007) using information on the PSF (e.g. FWHM) given in the SPIRE Observer's Manual⁸.

Our observations are dominated by confusion noise which is on the order of 6 – 7 mJy beam⁻¹ in the SPIRE photometric bands (Nguyen et al. 2010) as determined from deep extragalactic fields. In order to estimate the uncertainties due to confusion noise specifically in our target fields, we implemented the following procedure (see also Elbaz et al. 2011; Pascale et al. 2011): First, the source extractor was run over the full calibrated maps. Detections within less than half the FWHM from the

⁶ <http://herschel.esac.esa.int/twiki/bin/view/Public/PacsAotReleaseNotes>

⁷ <http://herschel.esac.esa.int/twiki/bin/view/Public/PacsCalibrationWeb>

⁸ http://herschel.esac.esa.int/Docs/SPIRE/html/spire_om.html

Table 2
Infrared photometry.

name	$F_{3.6\ \mu\text{m}}$ μJy	$F_{4.5\ \mu\text{m}}$ μJy	$F_{5.8\ \mu\text{m}}$ μJy	$F_{8.0\ \mu\text{m}}$ μJy	$F_{12\ \mu\text{m}}$ μJy	$F_{24\ \mu\text{m}}$ μJy	$F_{100\ \mu\text{m}}$ mJy	$F_{160\ \mu\text{m}}$ mJy	$F_{250\ \mu\text{m}}$ mJy	$F_{350\ \mu\text{m}}$ mJy	$F_{500\ \mu\text{m}}$ mJy
(1)	(2)	(3)	(4)	(5)	(6)	(7)	(8)	(9)	(10)	(11)	(12)
J0203+0012	80±1	88±1	106±6	106±7	353±111	680±44	< 3.3	< 5.4	< 15.6	< 13.5	< 18.0
J0338+0021	81±2	71±2	82±7	158±9	< 355	1187±52	10.7±1.0	18.5±2.0	19.6±5.9	18.5±6.2	12.6±6.5
J0756+4104	61±2	62±2	70±6	123±7	< 732	698±36	6.2±0.8	9.0±1.0	11.4±5.3	19.0±4.8	19.9±5.0
J0818+1722 ^a	168±2	200±2	167±8	216±10	425±127	1004±30	< 3.0	< 5.1	< 14.7	< 13.8	< 15.3
J0840+5624 ^b	58±1	80±1	61±7	62±6	...	440±29	< 2.7	< 4.2	< 15.3	< 13.5	< 15.3
J0927+2001	47±2	50±2	42±7	76±7	< 757	639±40	< 3.0	< 3.9	13.1±5.3	15.3±5.0	19.5±5.8
J1044-0125	106±2	131±2	108±8	186±9	< 398	1436±39	6.7±0.8	8.5±1.0	< 15.3	< 12.6	< 16.5
J1048+4637	110±2	120±2	95±7	128±7	< 315	818±41	< 2.1	< 3.0	< 14.4	< 14.1	< 18.6
J1148+5251 ^c	137±3	146±2	143±8	214±8	304±100	1349±39	3.9±0.6	7.4±1.7	21.0±5.3	21.8±4.9	12.4±5.7
J1335+3533	66±1	69±1	55±4	57±6	< 311	483±32	< 2.7	< 3.0	< 13.5	< 14.1	< 18.6
J2054-0005 ^d	< 18	< 48	< 162	< 1932	< 2.7	9.8±1.3	15.2±5.4	12.0±4.9	< 19.5

Note. — Upper limits correspond to 3σ . Photometry in columns (2)–(5) and (7) are from *Spitzer* observations, except for J2054–0005. Column (6) is based on data from the WISE All-Sky Survey. Columns (8)–(12) refer to *Herschel* data. **Notes:** (a) The *Spitzer* values of this source may include some contamination from a nearby galaxy (see text). The WISE observations do not separate the objects and the quoted catalog flux has to be taken with caution; (b) No $12\ \mu\text{m}$ photometry could be performed due to severe blending with bright nearby source; (c) This is the only source also observed at $70\ \mu\text{m}$ where we measure a flux of $2.9 \pm 0.6\ \text{mJy}$; (d) This object was not observed with *Spitzer*. Data in columns (2), (3), and (7) are based on aperture photometry on WISE All-Sky Survey atlas images at 3.4 , 4.6 , and $22\ \mu\text{m}$, respectively.

nominal target position were tentatively considered to belong to the quasar, pending further confirmation from our check for confusion with nearby FIR bright sources. We then created an artificial image which included all the sources found by the source extractor and subtracted this “source image” from the observed map. On this “residual map” we determined the pixel-to-pixel rms in a box with a size of 8 times the FWHM (FWHM size: $18.2''$, $24.9''$, and $36.3''$ for default map pixel sizes of 6, 10, and $14''$ at 250 , 350 , and $500\ \mu\text{m}$, respectively), centered on the nominal position of the QSO. The size of this box was chosen large enough to allow an appropriate sampling of the surroundings of the source, but small enough to avoid including the lower coverage areas at the edges of the map even for the longest wavelengths. In addition, the number of pixels per FWHM is approximately constant for the three wavelengths in the final maps ($2.5 - 3.0\ \text{px}/\text{FWHM}$) which translates into a similar number of pixels used for determining the rms in the background box. The resulting estimates for the noise (limited by confusion) are comparable to the average values given in Nguyen et al. (2010), but have a tendency to be slightly lower. The fluxes and uncertainties we determine are given in Table 2 and the $250\ \mu\text{m}$ maps are presented in Fig. 1.

We note that Table 2 lists a number of SPIRE flux measurements which are nominally below the estimated 3σ value of the noise. In these cases, the inspection of the images revealed a clear excess of flux at the position of the quasar. It has been shown that the use of positional priors can reduce the effect of confusion noise by 20–30% (Roseboom et al. 2010). While our strategy is somewhat different from that work, we benefit not only from accurate (relative and absolute) positional information, but also from information on the SEDs of the quasar and potential confusing sources in the field via our multi-wavelength data. This leads us to include these flux measurements in this study, although they have to be treated with caution. Similarly, fluxes at $500\ \mu\text{m}$ should be considered tentative because at this wavelength the beam is large ($\sim 36''$ FWHM), the confusion noise is high, and the significance of the detections is often low.

2.3. *Spitzer*

For all *Herschel* targets (except J2054–0005) we also have available mid-infrared (MIR) imaging from *Spitzer* at 3.6 , 4.5 , 5.8 , and $8.0\ \mu\text{m}$ with the InfraRed Array Camera (IRAC, Fazio et al. 2004) as well as at $24\ \mu\text{m}$ with the Multiband Imaging Photometer for *Spitzer* (MIPS, Rieke et al. 2004). For the redshifts of our sources these passbands cover the rest frame optical and near-infrared (NIR) wavelengths ($\sim 0.5 - 4\ \mu\text{m}$). The *Spitzer* data have been processed using standard procedures within the MOPEX software package provided by the *Spitzer* Science Center (SSC). Aperture photometry was performed in IDL using standard sets of aperture radii and appropriate aperture corrections as outlined in the respective instrument handbooks (also available from the SSC website). Errors were estimated in a similar fashion as for PACS by measuring the flux in randomly placed apertures on empty parts of the background and determining the variations between these background flux measurements. All objects in this paper with *Spitzer* data are detected at high significance in the five bands. The resulting photometry is summarized in Table 2 and is usually consistent with measurements published previously, where available (e.g. Jiang et al. 2006; Hines et al. 2006; Jiang et al. 2010). The $24\ \mu\text{m}$ images are presented alongside the PACS and SPIRE $250\ \mu\text{m}$ images in Fig. 1.

Our multi-wavelength data set, and in particular the *Spitzer* $24\ \mu\text{m}$ images, provide a tool for determining the exact position of the quasar in the *Herschel* bands. Since we can often identify several sources per field that are visible both at *Spitzer* and at *Herschel* wavelengths, the exact location of the quasar in the FIR maps can be determined from the relative positional information. With this procedure we can robustly identify faint *Herschel* detections with the quasars as well as avoid mis-identifications due to nearby objects. During this exercise we observe absolute spatial offsets between *Spitzer* and *Herschel* of typically $\lesssim 2''$, in line with expectations from the absolute pointing accuracies.

2.4. WISE

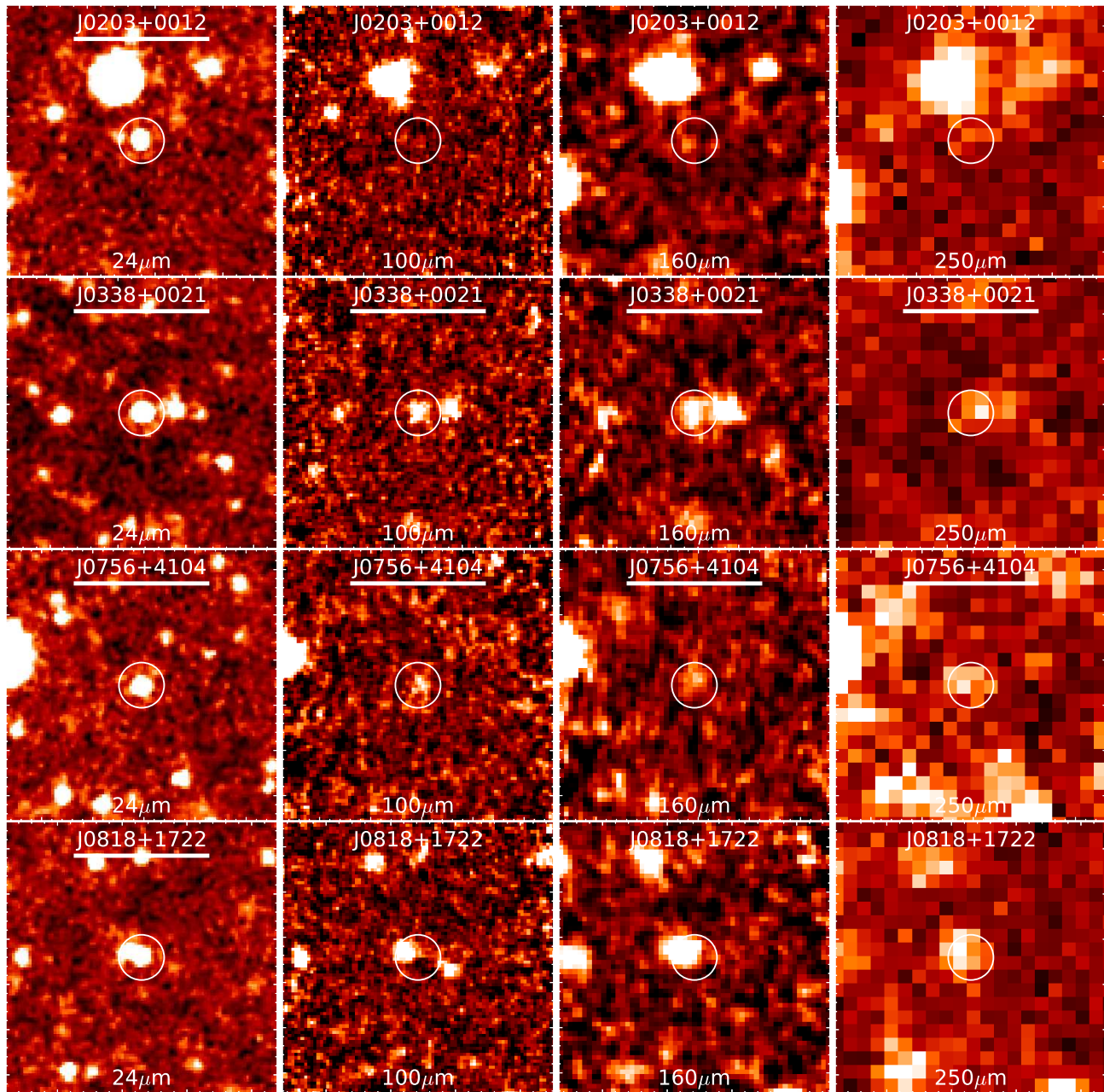


Figure 1. The final maps of the quasars at 24, 100, 160 and 250 μm (from left to right). All images are $2'$ on a side and North is to the top with East to the left. The circle indicating the position of the quasar has a diameter of $20''$. Sources detected in a particular band have their source name underlined in the corresponding image. In the case of J0818+1722 the bright source close to the QSO position at 100, 160, and 250 μm is identified with a foreground object. The QSO itself is undetected at these wavelengths (see the Appendix for details).

The all-sky data release of the Wide-field Infrared Survey Explorer (WISE; Wright et al. 2010) was queried for photometry or upper limits in the $12\ \mu\text{m}$ band which can fill the gap in the *Spitzer* photometry between 8 and $24\ \mu\text{m}$. Only three quasars in this paper are detected at $12\ \mu\text{m}$ and their significance is low ($\lesssim 3.5\sigma$, Tab. 2). Some objects (e.g. J2054–0005) are not detected in any WISE band, and consequently no upper limits are available in the point-source catalogue. For such sources we performed aperture photometry on the WISE atlas images to determine upper limits, following the guidelines in the explanatory supplements to the WISE All-Sky Data Release Products (Cutri et al. 2012).

2.5. Supplemental data

Additional data from the literature was compiled, mainly in the observed NIR or mm regimes and often taken from the discovery papers. The latest data release of the UKIDSS survey (Lawrence et al. 2007) was also checked which yielded additional photometry in the NIR for six objects.

3. ANALYSIS

3.1. SED components

In combination with other supplemental data from the literature (section 2), we compile SEDs covering a rest frame wavelength range of typically $0.1\text{--}400\ \mu\text{m}$ (see Figs. 2 and 3). These SEDs are then fitted with a com-

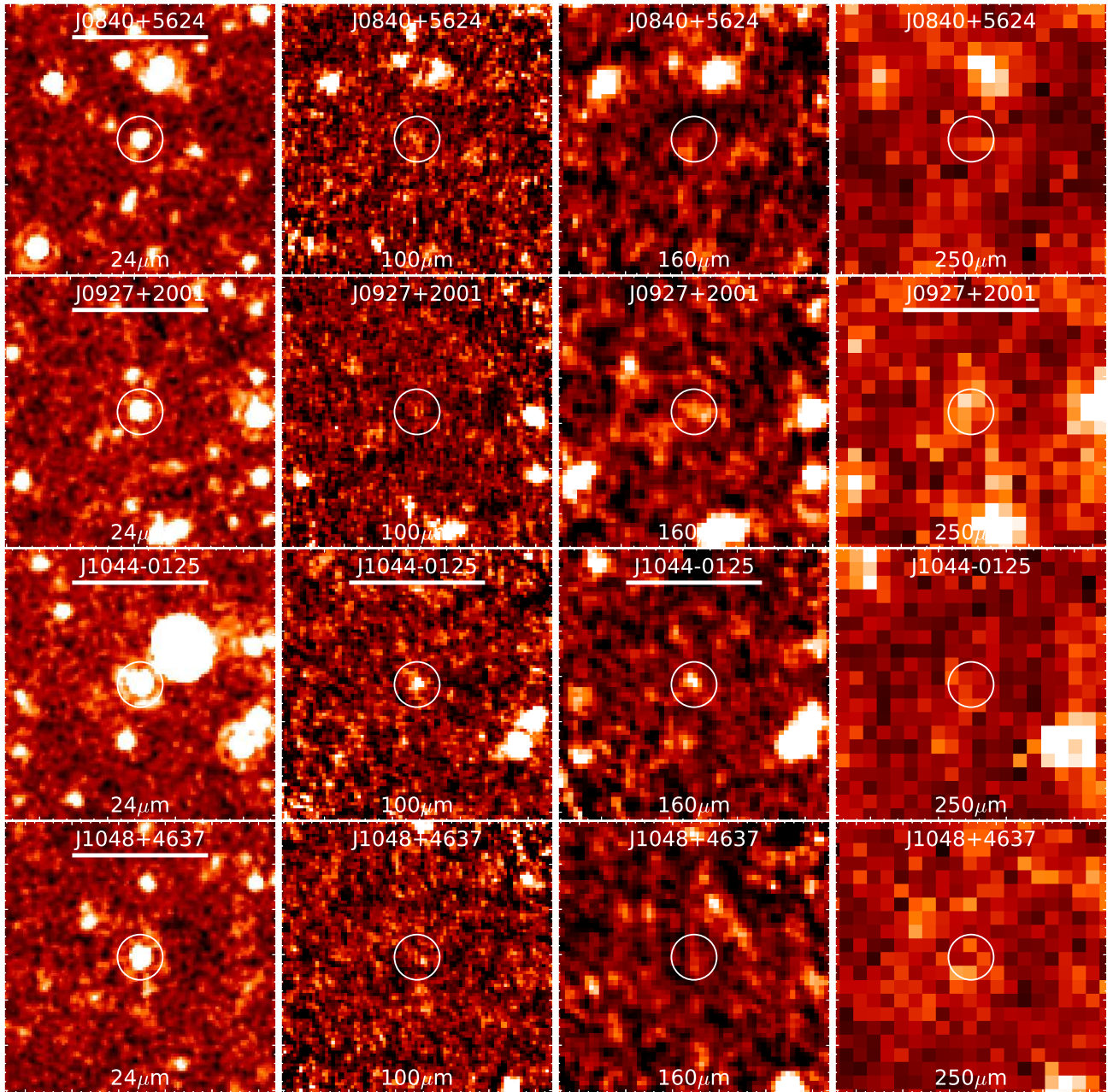


Figure 1. *continued*

bination of models to represent the different components contributing to the observed SED. For this purpose we have divided our sample into two groups, depending on the amount of data available to constrain the fitted components. Objects detected in at least two *Herschel* bands were subject to full SED fits (five sources), except J2054–0005, for which the lack of strong photometric constraints at rest frame wavelengths $< 10 \mu\text{m}$ (no *Spitzer* observations and only WISE upper limits) prevented a full SED fit. In our fits we consider four distinct components:

1. A power law in the UV/optical regime which represents the emission from the accretion disk. We extend this component into the NIR and introduce a break to a the Rayleigh-Jeans slope of $F_\nu \propto \nu^2$ at $3 \mu\text{m}$ in the rest frame (Hönig & Kishimoto 2010). In the fitting, the power-law slope in the UV/optical and the overall normalization are free parameters.
2. A blackbody of typically 1300 K temperature, thus peaking in the restframe NIR. Empirically, such a component is often required to fit the optical through MIR SEDs of luminous quasars (e.g. Barvainis 1987; Gallagher et al. 2007; Mor et al. 2009; Leipski et al. 2010a) and is generally interpreted as a signature of hot (graphite) dust close to the sublimation temperature.
3. A clumpy torus model from the library of Hönig & Kishimoto (2010) to account for the AGN heated dust from the “dusty torus” in the central parts of the AGN. This component dominates the MIR and

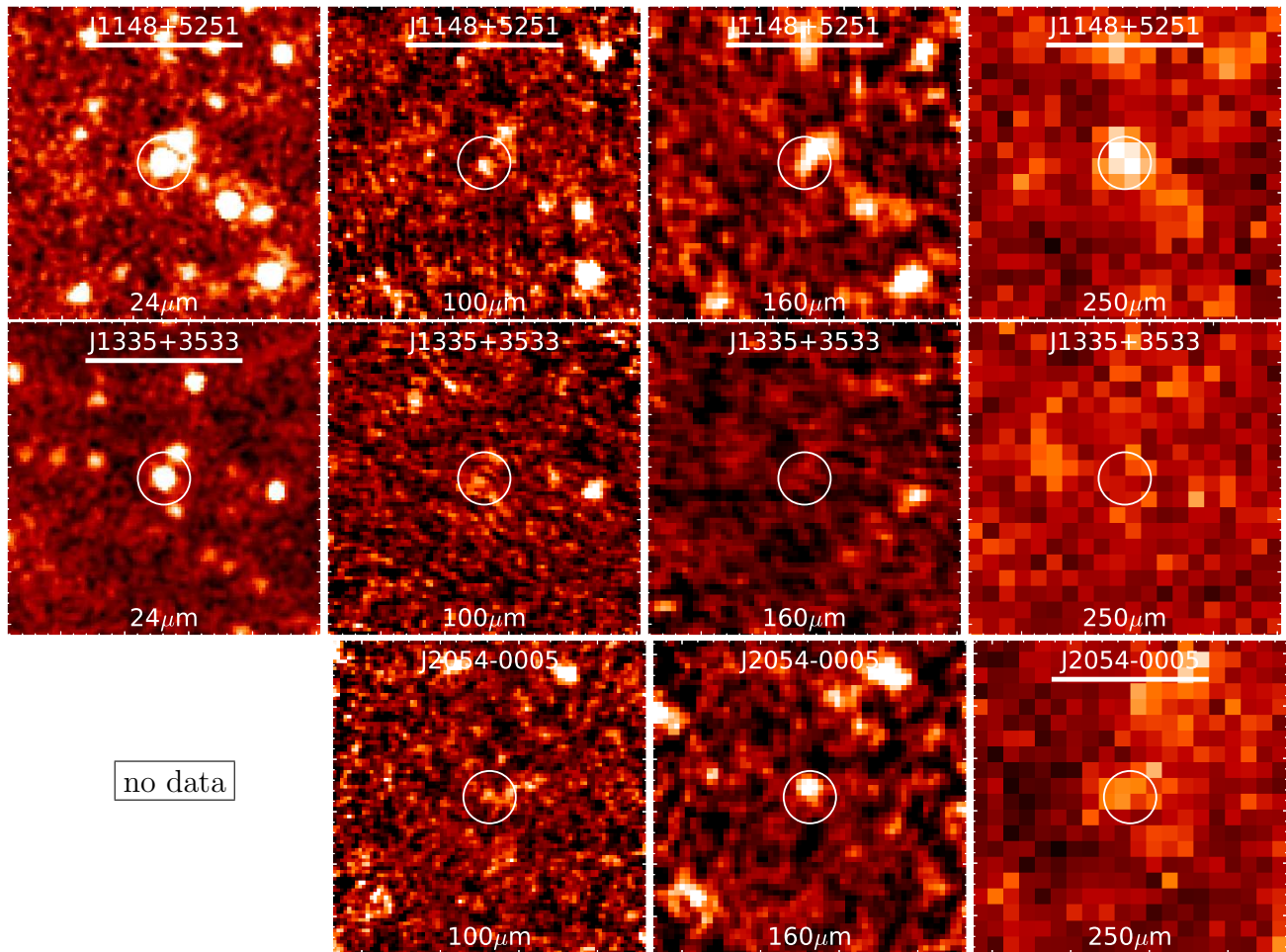


Figure 1. *continued*

is important to disentangle, to first order, the contributions from the nuclear dust to the rest frame FIR emission. Besides the choice of a particular model (see below), the absolute scaling of the model is the only free parameter for this component.

4. A modified black body to account for possible FIR excess emission (over the AGN heated torus) which we here interpret as powered by star formation. For this component we fix the emissivity index β to a value of 1.6 (e.g. Beelen et al. 2006; Wang et al. 2008a, but see section 4.3). The temperature of the modified black body and the normalization are free parameters.

3.2. Fitting procedure

The torus models we consider here are available for seven different inclinations (starting at 0° and increasing in steps of 15°). For each inclination, Hönig & Kishimoto (2010) provide models of various combinations of parameters (opening angle, radial dust distribution, etc.). Our fitting procedure takes one of the torus models and fits a linear combination of the four components to the observed SED via chi-square minimization using MPFIT (Markwardt 2009) in IDL. We then cycle through all torus models in the library and repeat the fitting for each

of them. However, for efficiency we limit the torus component to models with inclinations ≤ 45 degrees which seems reasonable given that we observe luminous and largely unreddened type-1 quasars. This leaves a total of 959 different torus models. We visually inspect the best-fitting 10% of the model combinations to confirm the fits.

With this approach we do not intend to develop a highly accurate model for the full SED emission in these objects. For the current work we aim to construct a physically motivated approximation that yields a reasonable description of the observed SEDs which allows us to isolate excess FIR emission and to account for (to first order) contributions of the AGN heated nuclear dust to the FIR photometry.

As outlined above, our fitting includes an additional, empirically motivated 1300 K black body in the NIR. We have also performed the fits excluding this component, only fitting a power-law, a torus model and a FIR modified black body. The comparison between both cases shows that the fits including the NIR black body generally represent the observed photometry better. This is particularly apparent in wavelength regions dominated by very hot dust ($\lambda_{\text{rest}} \sim 1\text{-}3 \mu\text{m}$), in the overlap region between the torus and the FIR black body ($\lambda_{\text{rest}} \sim 20\text{-}30 \mu\text{m}$) and in the fit at $\lambda_{\text{rest}} \gtrsim 100 \mu\text{m}$. The temperatures of the FIR dust component also come out consistently lower (by about 5-10 K) in fits including the additional

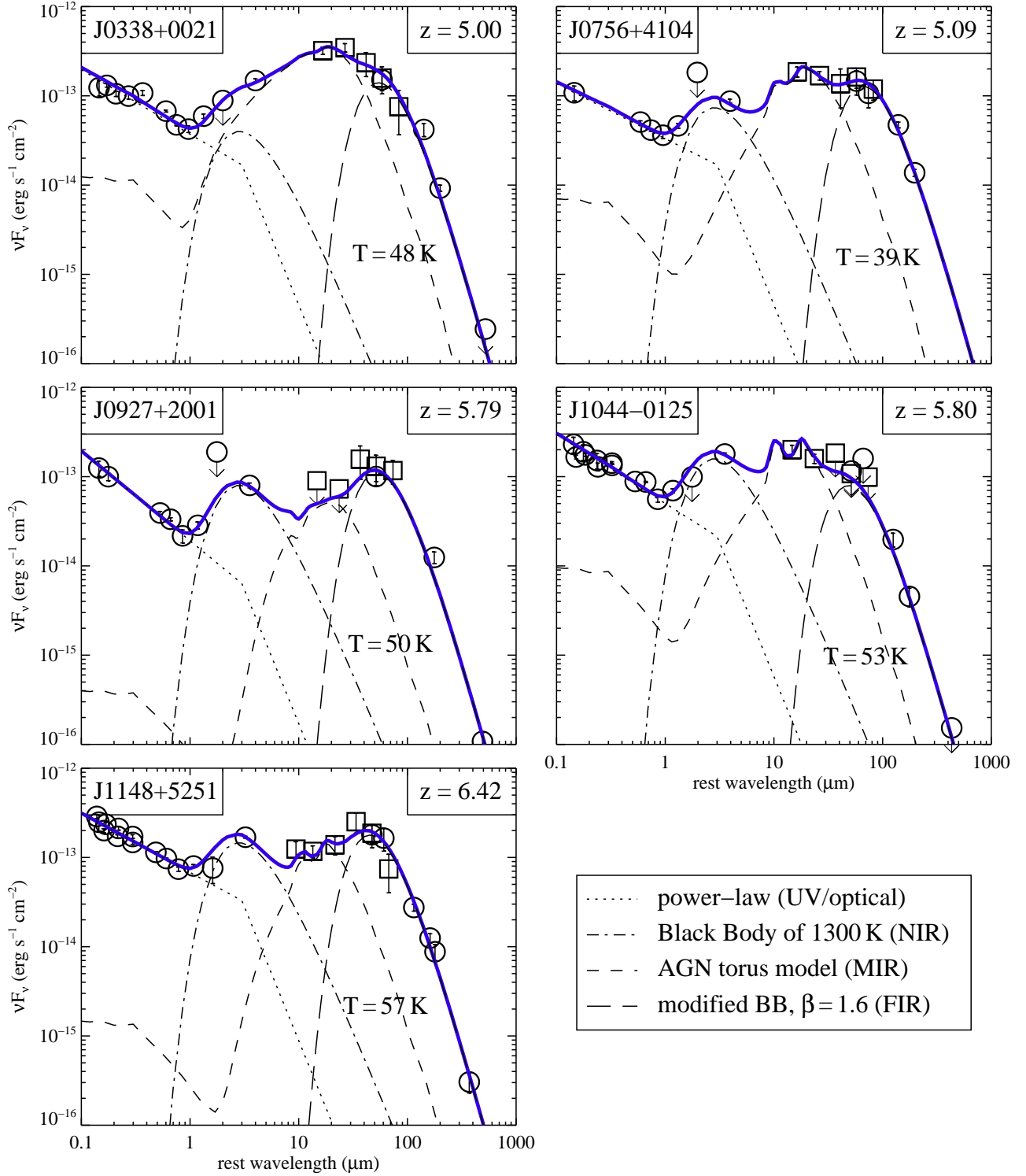


Figure 2. Observed SEDs of mm-detected quasars with at least two *Herschel* detections; for these objects multi-component SED fits were carried out as outlined in section 2. The SED fit is performed using a power-law in the UV/optical (dotted line), a 1300 K black body in the NIR (dot-dashed line), a torus model in the NIR/MIR (short dashed line) and a modified black body in the FIR with emissivity index β fixed to 1.6 (long dashed line). The blue solid line corresponds to the sum of the fitted components which here represent the overall best fit. Thus, the temperature of the FIR component here may differ slightly from the overall mean temperature determined from all acceptable fits as presented in Tab. 3. The squares correspond to the new *Herschel* data.

NIR black body.

Recall that the additional NIR component contributes significantly (or dominantly) to the short infrared wavelengths. In cases where this component is absent, torus

models with a strong emphasis on emission at $\lambda \lesssim 10 \mu\text{m}$ are favored in the fits to accommodate (in particular) the MIPS photometry. By design such torus models contribute less flux at longer wavelengths ($\lambda \gtrsim 20 \mu\text{m}$) thus

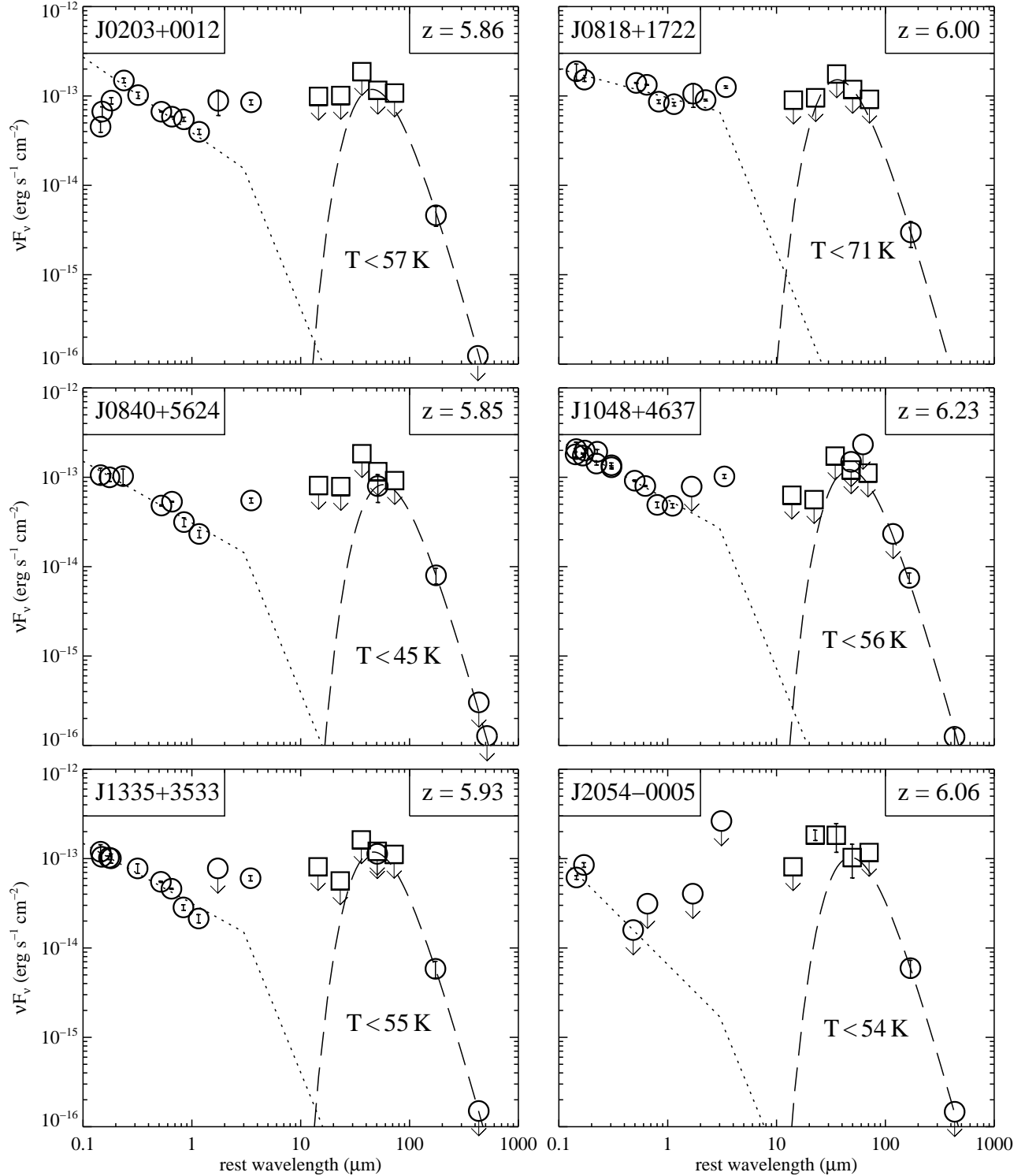


Figure 3. Observed SEDs of mm-detected quasars without *Herschel* detections. Despite SPIRE detections, the object J2054–0005 is included here because the poor constraints on the rest frame optical through MIR SED prevents detailed SED fits.

requiring a hotter FIR component to match the *Herschel* photometry. This in turn negatively affects the fit in the observed sub-mm/mm regime. Including the NIR component, more power in the torus component can shift to slightly longer wavelengths, allowing a cooler FIR component and providing a better overall fit to the data. The need to add an additional hot component to torus mod-

els when fitting type-1 AGN SEDs has also been noted by e.g. Mor & Netzer (2012). NIR reverberation mapping observations (e.g. Suganuma et al. 2006) show that the size of the emitting region of this very hot dust is a factor of ~ 20 smaller than the torus as measured in the MIR via interferometry (Burtscher et al., in preparation), supporting this additional complexity in the distribution

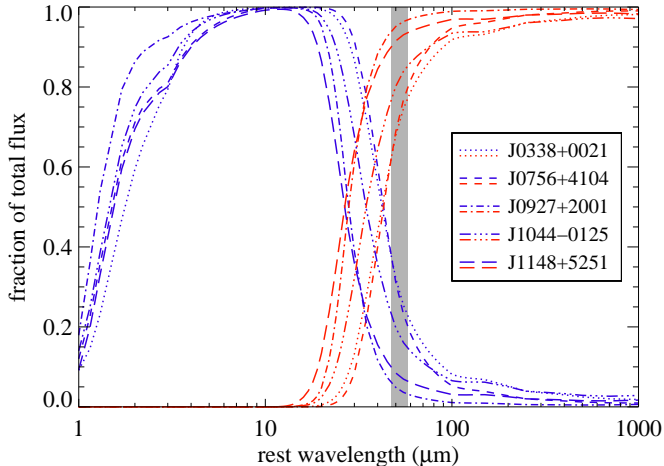


Figure 4. Relative contributions of the NIR bump plus torus emission (presumably AGN-powered; blue) and the FIR black body (presumably star-formation powered; red) to the total SED fit as a function of wavelength. The vertical grey bar indicates the wavelength range sampled by the observed $350\ \mu\text{m}$ band for the redshifts of the sources in this plot ($z = 5.0 - 6.4$).

of the AGN-heated dust. The following results and discussion will therefore be based on the fits including the additional NIR black body.

4. RESULTS

4.1. Detection rates

In our new *Herschel* observations we detect six out of eleven sources (Tab. 2). Typically, the quasars are either detected in all five bands or not at all with *Herschel*. This is an important point which will be revisited in section 5.2. The exceptions are J0927+2001 which is detected with SPIRE but not with PACS and J1044-1025 for which the opposite is the case.

From the ten objects observed with *Spitzer*, all are detected in all bands. With WISE at $12\ \mu\text{m}$ only three objects are detected and at low significance. More detailed information on the individual objects can be found in the Appendix.

4.2. The temperature of the FIR dust

Previous studies of star formation in high-redshift ($z > 5$) quasars often had to rely on single band mm emission as a tracer for the starburst heated dust (e.g. Bertoldi et al. 2003; Wang et al. 2008a). Far-infrared luminosities were determined by fitting a single modified black body to the mm photometry and integrating under this component. Since no knowledge about the temperature of the dust was at hand for most cases, typical values found for FIR bright quasars at lower redshift ($z \sim 2-4$) were assumed (e.g. $T = 47\ \text{K}$, $\beta = 1.6$; Beelen et al. 2006). This approach has been tentatively supported for some high-redshift quasars by ground-based observations at $350\ \mu\text{m}$ (Wang et al. 2008b, 2010).

The new multi-wavelength FIR photometry now allows us to estimate the temperature of the FIR emitting dust directly while simultaneously accounting for the contributions from AGN heated nuclear dust to the infrared. In Figure 2 we present the SEDs of the five objects which are detected in at least two *Herschel* bands and their accompanying best fits.

As explained above, details of the SED of the AGN

heated dust torus affects the shape (and temperature) of the FIR component. We have taken this into account when calculating the uncertainties of the dust temperature (see section 4.5). The values of T_{FIR} we obtain here for these five objects are reported in Table 3. We clearly see a range of temperatures among these objects, spanning almost 20 K.

One important result from the SED fits in Figure 2 is that the flux at $\lambda_{\text{rest}} \gtrsim 50\ \mu\text{m}$ is usually dominated by the FIR excess emission with only minor contributions from the AGN heated torus. This is further illustrated in Fig. 4 where we show the fractional contribution of the hot dust plus dusty torus component (both presumably powered by the AGN) compared with the contributions from the FIR excess component, which may be powered by star formation. As indicated in this figure, the SPIRE $350\ \mu\text{m}$ band is typically dominated by emission from the FIR black body for the redshifts considered here. In fact, fitting only a single modified black body ($\beta = 1.6$) to the photometry at $\lambda \geq 350\ \mu\text{m}$ gives very similar dust temperatures compared to the full SED fits.

This result can immediately be utilized for an estimate on the dust temperature for objects which do not qualify for full SED fits (see Figure 3). In these cases we use the 250 GHz detection as an anchor for the (modified) black body while the FIR upper limits at $\lambda \geq 350\ \mu\text{m}$ (mostly from SPIRE) allow us to constrain the maximum permitted temperature of this component. Because of our findings from the full SED fits (Fig. 4) we can assume that our upper limits to the dust temperature are reasonably robust when limiting the fits to $\lambda \geq 350\ \mu\text{m}$, even without suitable constraints on the AGN dust emission in these objects. We determine dust temperatures of $\leq 57\ \text{K}$, with J0818+1722 being the only exception ($T_{\text{FIR}} \leq 71\ \text{K}$). However, the latter value has to be taken with caution because the 250 GHz photometry of this source could be contaminated by the emission from the nearby galaxy that is detected in most infrared bands (see notes on individual objects in the Appendix and Figure 1).

4.3. The emissivity index β

In the previous fits, the emissivity index β was fixed to a value of 1.6 to enable the comparison with earlier literature studies. The good photometric coverage in the FIR and sub-mm for some of our objects now allows us to explore in how far β can be constrained using the quasar SEDs. For such a study, additional photometry at lower frequencies (typically around 90 GHz in the observed frame) is very important as it helps to further constrain the Rayleigh-Jeans tail of the fitted dust component. In fact, considering only photometry at $\nu_{\text{obs}} > 250\ \text{GHz}$ does not provide good constraints on β (or the FIR dust temperature) if both parameters are kept free during fitting. Photometry at $\sim 90\ \text{GHz}$ in combination with *Herschel* FIR detections is available for four objects in our sample. Re-fitting the SEDs as outlined previously but now keeping β as a free parameter, we find relatively high β values (2.0 - 2.7) combined with relatively low temperatures ($\sim 33\ \text{K}$, but still 54 K for J1148+5251). The integrated luminosity of the FIR dust when determined from these new fits remains virtually unchanged as compared to a fixed β approach. We caution, however, that a reliable measure of β is hard to obtain in these objects

because the peak of the dust emission is not well defined (or isolated) in the SED due to the strong nuclear dust emission from the torus. Therefore, the peak wavelength (and temperature) of the FIR black body depends on the choice of the torus model which adds additional uncertainty in the determination of β .

4.4. Far-infrared luminosities, star-formation rates and dust masses

Integrating the emission of the FIR excess component only (i.e. the modified black body) between 8 and $1000 \mu\text{m}$ in the rest frame allows us to determine its luminosity L_{FIR} . The FIR luminosities we derive are of the order of $\sim 10^{13} L_{\odot}$ (see Tab. 3), which corresponds to $\sim 25\text{-}60\%$ of the bolometric FIR luminosity in these objects. For sources with full SED fits, the values for L_{FIR} do not change significantly ($\lesssim 10\%$) if we fit only a single modified black body to the photometry at $\lambda_{\text{obs}} \geq 350 \mu\text{m}$.

Assuming that the FIR emission is powered by star formation, we converted the FIR luminosities into star-formation rates using the formula in Kennicutt (1998). The results are reported in Table 3. Using our fits of the FIR excess component we can also derive an estimate for the dust masses in the star forming regions:

$$M_{\text{dust}} = \frac{S_{250\mu\text{m}} D_L^2}{\kappa_{250\mu\text{m}} B_{\nu}(250\mu\text{m}, T_{\text{FIR}})} \quad (1)$$

where $S_{250\mu\text{m}}$ is flux level at a rest frame wavelength of $250 \mu\text{m}$ as determined from the fit, D_L is the luminosity distance, $\kappa_{250\mu\text{m}}$ is the dust absorption coefficient at $250 \mu\text{m}$ as determined from the models of Draine (2003), and $B_{\nu}(250\mu\text{m}, T_{\text{FIR}})$ is the value of the Planck function with temperature T_{FIR} at a wavelength of $250 \mu\text{m}$. The results are also reported in Table 3.

4.5. Error estimates on physical parameters

In order to estimate uncertainties in the derived parameters we studied the distribution of their values resulting from all the fitted models ($N \sim 1000$; as outlined in section 3.2 we only include torus models with inclinations of ≤ 45 degrees). This also allows us to account for the influence the choice of a particular torus model has on these parameters.

As a first step, we calculated for all the fitted models the residuals between the global fit and the observed data in the infrared ($\lambda_{\text{rest}} > 1 \mu\text{m}$) and determined the error-weighted RMS for these points. A typical distribution of the resulting RMS values is presented in panel '(a)' of Figure 5 (we here use the quasar J0756+4104 as an example to demonstrate our approach). In this figure we see a clear peak at low RMS values representing a family of good fits, with an extended tail to large RMS values corresponding to increasingly worse model representations of the observed SED. We then fitted the right side of the RMS peak with a Gaussian (dashed line). All fits with an RMS value within 3σ of the centroid value of the Gaussian are identified as acceptable model fits. The values corresponding to these fits are marked as blue and hashed regions in all panels of Figure 5 and are used for estimating uncertainties on the derived values.

Each of the $N \sim 1000$ model fits provides a value for the temperature of the modified black body in the FIR (T_{FIR} , panel '(b)' in Fig. 5). From the temperature and

the normalization of this component we can then calculate (see section 4.4) L_{FIR} (panel '(c)'), a star-formation rate (panel '(d)'), and a dust mass M_{dust} (panel '(e)'). In each histogram we fit the parameter values obtained from the acceptable fits (as determined from the residual RMS distribution; blue and hashed regions) with a Gaussian (dashed line). This gaussian fit provides us with a mean parameter value (centroid) and an uncertainty (σ) for each fitted object. These results are reported in Tab. 3.

5. DISCUSSION

5.1. Comparison with previous studies

The average temperature of the modified black body used to model the FIR emission is comparable to the ~ 47 K measured for lower redshift FIR bright quasars (Beelen et al. 2006). This finding is confirmed by the average SEDs presented in section 5.2 below.

While this is true on average, we see a significant spread in dust temperature (~ 20 K) between individual objects, even for comparable FIR luminosities. Despite the low number of objects for which such fits can be performed, this finding highlights that the choice of the dust temperature can add uncertainty to the estimate of L_{FIR} and M_{dust} , in particular for objects with only single photometric measurements and thus no individual constraints on T_{FIR} .

A related issue is that of possible AGN contributions to the heating of the FIR dust which will be discussed briefly in the following section.

We also find that in our modeling strategy the FIR component can be isolated from the torus component if only data at $\lambda_{\text{rest}} \gtrsim 50 \mu\text{m}$ are considered (see section 4.2 and Fig. 4). Consequently, single-component fits to data at these wavelengths yield estimates of the FIR luminosity, temperature and dust mass that match the values based on the full SED fits. This result validates the approach in previous studies of high- z quasars (Bertoldi et al. 2003; Beelen et al. 2006; Wang et al. 2008a,b) in which single-component fits to (ground-based) photometry at $\lambda_{\text{obs}} \geq 350 \mu\text{m}$ was used to derive physical parameters (with the caveat of unknown dust temperature in some of these studies). It also adds further significance to the upper limits on T_{FIR} , L_{FIR} , and SFR we determine for the remainder of our sample where we are limited to single component fits at $\lambda_{\text{obs}} \geq 350 \mu\text{m}$.

The strong overlap between the torus and the FIR components in our fits does not provide good constraints on the emissivity index β of the latter component. The difficulty of determining reliable β estimates in objects with a strong AGN is also apparent from the literature: Priddey & McMahon (2001) find a high β value of ~ 2 (with a FIR dust temperature of 41 K) by combining the available photometry for a number of $z \sim 4$ quasars into a single SED and using this global SED to constrain a modified black body fit. On the other hand, using a similar approach (and much of the same data), Beelen et al. (2006) find $\beta \sim 1.6$ and $T_{\text{FIR}} \sim 47$ K for a sample of quasars with $z = 1.8 - 6.4$.

5.2. Stacking of the FIR data

In order to better constrain the FIR emission of the SPIRE non-detected objects, we stacked the individual SPIRE observations at the nominal position of the

Table 3
Physical parameters derived from the fitted components.

name	$\alpha_{UV/opt}$	$L_{UV/opt}$ $10^{46} \text{ erg s}^{-1}$	$L_{NIR/MIR}$ $10^{46} \text{ erg s}^{-1}$	T_{FIR} K	L_{FIR} $10^{13} L_{\odot}$	% of L_{FIR}	SFR $10^3 M_{\odot} \text{ yr}^{-1}$	M_{dust} $10^8 M_{\odot}$
(1)	(2)	(3)	(4)	(5)	(6)	(7)	(8)	(9)
J0203+0012	-0.16 ± 0.02	9.6 ± 0.2	<10.5	<57	<1.3	...	<2.2	...
J0338+0021	-0.39 ± 0.03	4.8 ± 0.3	18.1 ± 0.9	47 ± 4	1.1 ± 0.4	24	1.8 ± 0.6	6.8 ± 2.0
J0756+4104	-0.42 ± 0.03	4.1 ± 0.3	10.3 ± 0.3	40 ± 2	1.1 ± 0.2	35	1.9 ± 0.3	15.9 ± 1.6
J0818+1722 ^a	-0.68 ± 0.02	12.5 ± 0.2	<8.3	<71	<1.8	...	<3.1	...
J0840+5624	-0.31 ± 0.02	6.1 ± 0.2	<8.8	<45	<0.9	...	<1.6	...
J0927+2001	0.00 ± 0.03	5.5 ± 0.2	<7.3	50 ± 2	1.3 ± 0.2	62	2.1 ± 0.3	5.3 ± 0.4
J1044-0125 ^b	-0.33 ± 0.03	9.9 ± 0.3	19.3 ± 0.5	<53	<1.2	<24	<2.1	...
J1048+4637	-0.33 ± 0.02	12.4 ± 0.2	<11.5	<56	<1.6	...	<2.7	...
J1148+5251	-0.35 ± 0.03	15.3 ± 0.2	16.6 ± 0.9	59 ± 3	2.7 ± 0.3	54	4.6 ± 0.5	4.7 ± 0.6
J1335+3533	-0.33 ± 0.02	6.3 ± 0.2	<7.3	<55	<1.4	...	<2.4	...
J2054-0005	-0.22 ± 0.02	3.0 ± 0.2	<22.5	<54	<1.3	...	<2.2	...

Note. — (2) Power-law slope in the UV/optical ($F_{\nu} \sim \nu^{\alpha}$); (3) Integrated luminosity between 0.1 and $1 \mu\text{m}$ of the power-law component; (4) Integrated luminosity between 1 and $1000 \mu\text{m}$ of (presumably) AGN powered dust emission (NIR black body and torus component combined); (5) Temperature of the modified black body fitted in the FIR; (6) Integrated luminosity between 8 and $1000 \mu\text{m}$ of the star-formation powered FIR component; (7) Percentage contribution of star formation to total FIR luminosity between 8 and $1000 \mu\text{m}$; (8) Star-formation rate derived from $L_{FIR,SF}$ using Kennicutt (1998); (9) Dust mass derived from the star-formation powered FIR component following equation 1.

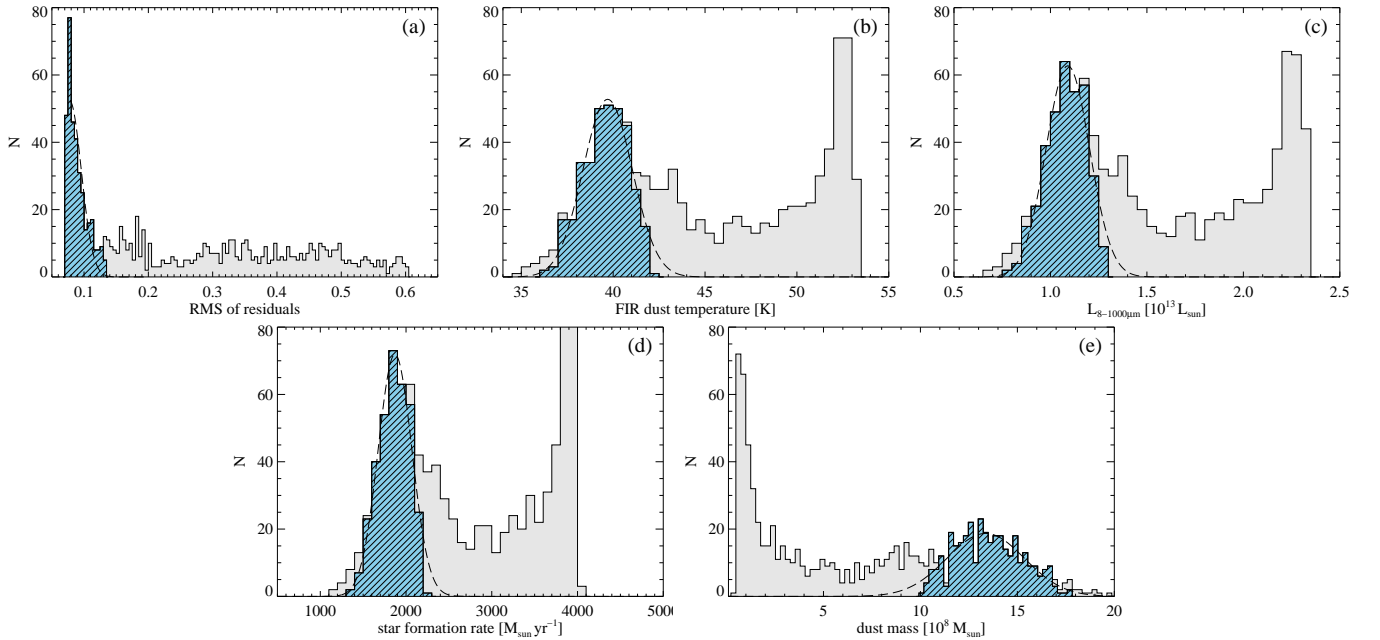


Figure 5. Histograms of derived values from the SED fits of the quasar J0756+4104. The grey shaded area in each panel shows the $N \sim 1000$ solutions from all fits, while the blue and hashed region identifies values based on acceptable fits (see text). The dashed lines in each panel represent Gaussian fits to the data from the acceptable fits. Panels (d) and (e) rely on the assumption that the FIR emission is powered by star formation.

quasar (excluding J0818+1722 due to possible confusion issues)⁹. Even in the stacked images no significant detection was achieved (see Fig. 6). Stacking the corresponding PACS data we recover a faint ($\sim 3\sigma$) average signal at 100 and $160 \mu\text{m}$. We iterated during the stacking, leaving a different source out of the stack for every iteration to verify that the result is not biased by any individual object. Differences between these stacks were usually smaller than the uncertainty on the photometry of the total stack. The photometry was performed in an identical manner to the individual frames and as outlined in section 2.

⁹ We also excluded J1044-0125 from this stack. While the source is also not detected with SPIRE, its PACS detection would influence the average PACS flux of this subsample significantly.

Using the stacked *Herschel* fluxes and combining them with stacked WISE data as well as averaged *Spitzer* and mm photometry, we can produce an average SED for the FIR non-detected objects which is presented in Fig. 7. Performing the same stacking/averaging procedure for the objects detected in the FIR individually (excluding J1148+5251 due to possible confusion issues) also provides us with an average SED for these objects.

Fitting the average FIR SEDs with a modified black body (at $\lambda_{\text{obs}} \geq 350 \mu\text{m}$, $\beta = 1.6$) reveals dust temperatures of 47 K for the stack of the individually detected objects, as expected considering the individual FIR dust temperatures of the objects in this stack (Tab. 3). For the average SED of the objects individually undetected in SPIRE we determine an upper limit of 49 K which

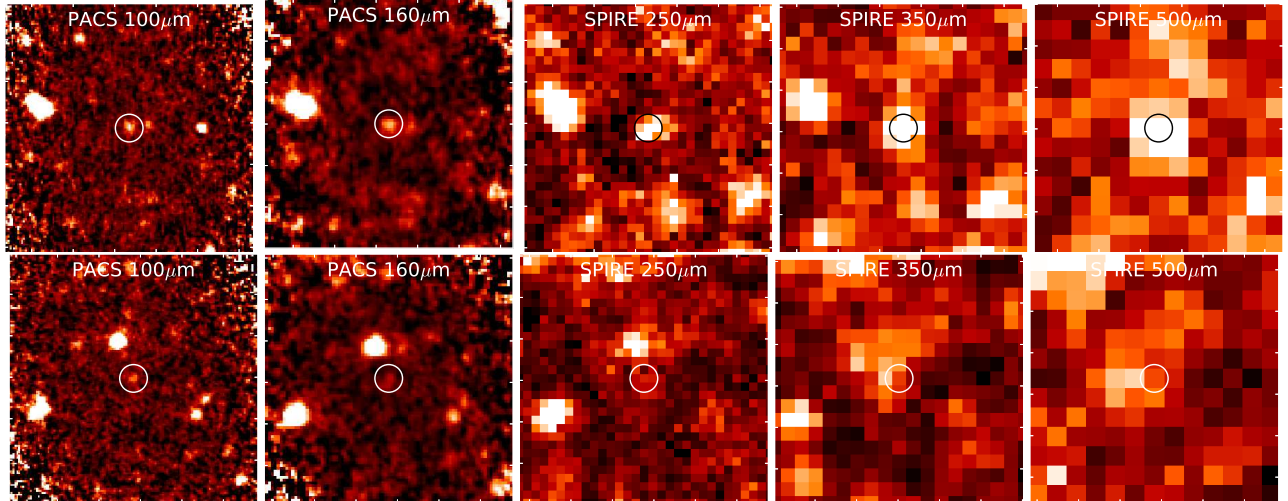


Figure 6. Stacked *Herschel* images of sources with individual SPIRE detections (top row) and without individual SPIRE detections (bottom row). The images are $3'$ on a side and the circle indicates the center of the stack and has a diameter of $20''$.

is lower than the upper limits determined individually (Tab. 3). These temperatures are very similar to the values commonly adopted for mm detected quasars with only few or single photometric data points (e.g. Beelen et al. 2006; Wang et al. 2008b). They also agree well with the dust temperatures observed for sub-mm galaxies of comparable FIR luminosity (Magnelli et al. 2012).

In Fig. 7 we also compare our average SEDs with the SDSS quasar template of Richards et al. (2006). When normalized at $1\ \mu\text{m}$ (using a power-law fit to the rest frame UV/optical emission), we see that below $\sim 30\ \mu\text{m}$ the average SED of the SPIRE non-detections (blue points in Fig. 7) looks similar to the typical SDSS quasar template. At longer wavelengths we see an additional cool dust component for our sources, as indicated by the available mm observations. Not considering these longer wavelengths, we see AGN powered emission with possibly increased emphasis on the hottest dust (NIR) when compared to the template.

In contrast, for a similar scaled UV/optical emission, the average infrared SED of the SPIRE detected quasars (red points in Fig. 7) exceeds the scaled template significantly at any wavelength $\lambda_{\text{rest}} \gtrsim 1\ \mu\text{m}$. This includes the presumably AGN powered dust emission at short infrared wavelengths ($\lambda_{\text{rest}} \lesssim 20\ \mu\text{m}$) as well as the FIR emission possibly powered by additional star formation.

The observed discrepancy between the average SEDs in Figure 7 is somewhat puzzling. Both groups of objects have similar UV/optical properties (on average), indicating that their black holes grow at comparable rates. Now, assuming that the NIR and MIR emission is powered by the AGN, the objects with individual *Herschel* detections (red symbols) convert a higher fraction of their accretion luminosity into re-processed dust emission. This could, in principle, be caused by a different dust geometry (or dust content) in the inner parts of these objects. This in turn could also lead to increased contributions of AGN powered dust emission at FIR wavelengths. If AGN-powered dust emission extends further into the FIR than anticipated by the torus models we utilize here, the values for the inferred star-formation luminosity (and star formation rates) in these objects (Tab. 3) would be overestimated.

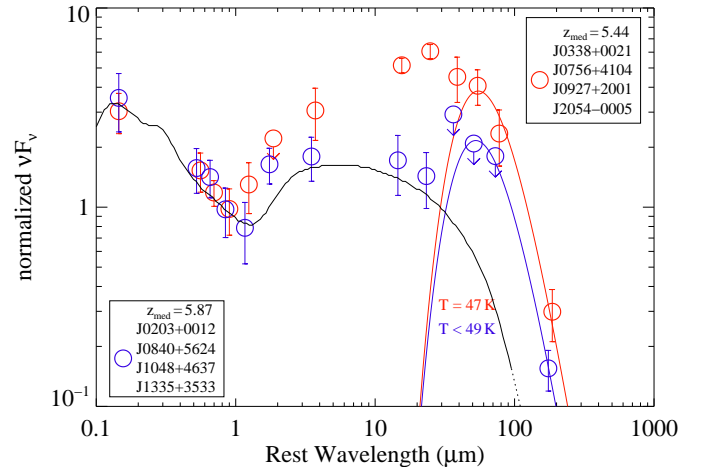


Figure 7. Average SEDs of mm-detected quasars with individual FIR detections (red) and without individual FIR detections (blue). The solid colored lines represent modified black body fits ($\beta = 1.6$) to the observed photometry at $\lambda > 350\ \mu\text{m}$. The solid black line shows the mean SDSS quasar template presented in Richards et al. (2006), matched in the UV/optical and extended by a power law of $F_\nu \propto \nu^{-2}$ at the longest wavelengths. All SEDs shown here were normalized at a rest frame wavelength of $1\ \mu\text{m}$.

While a detailed discussion of this issue is beyond the scope of this paper, it is worth keeping in mind that the AGN may be contributing to the heating of the FIR dust depending on the dust distribution and geometry.

6. SUMMARY AND CONCLUSIONS

New *Herschel* observations of eleven $z > 5$ quasars with detections at $1.2\ \text{mm}$ are combined with data at other wavelengths to analyze their full SEDs covering the rest frame wavelength range of $\sim 0.1\text{--}400\ \mu\text{m}$. Our results can be summarized as follows:

- Six out of the eleven objects are detected in at least two of the five *Herschel* bands. Five of them have sufficient data coverage and quality to allow full SED fits.
- In all cases where such fits could be performed, AGN powered emission from a dusty torus is not

sufficient to explain the observed FIR fluxes. An additional FIR component is required to model the SEDs. Similar to other studies of luminous (but lower redshift) quasars, we notice the need for a hot (~ 1300 K) dust component to account for the strong rest frame NIR emission.

- The additional FIR component was modeled as a modified black body and shows temperatures of $T \sim 40$ -60 K. We interpret this emission as being powered by star formation with luminosities of $L_{8-1000\mu\text{m}} \sim 10^{13} L_{\odot}$ which translate into star-formation rates of several thousand solar masses per year.
- Our fits also allow us to estimate that the contributions of the AGN powered dust to the infrared SED are small at wavelengths $\lambda_{\text{rest}} \gtrsim 50 \mu\text{m}$. For the redshifts of our objects this implies that the star-formation powered FIR component can be isolated and characterized adequately by single component fits if only photometric measurements at $\lambda_{\text{obs}} \gtrsim 350 \mu\text{m}$ are considered. This explains the good match for the temperature and luminosity of the FIR emission with previous studies of such objects which relied on (ground-based) observations at $\lambda_{\text{obs}} \gtrsim 350 \mu\text{m}$.
- By stacking the *Herschel* data of individually undetected sources we recover a signal in PACS but not in SPIRE. We use this stacking approach to construct average SEDs for objects with and without

individual *Herschel* detections. We find that the high-redshift objects which are individually undetected with *Herschel* show an SED similar to quasar templates constructed from lower redshift and lower luminosity objects.

- The average SED of the *Herschel* detected objects, on the other hand, shows a surplus of NIR and MIR emission relative to the UV/optical when compared to the *Herschel* nondetections or to quasar templates. This may suggest a correlation between strong FIR emission (here modeled as star-formation powered) and strong MIR emission (here modeled as AGN powered), and possibly indicates significant AGN contributions to the FIR emission.

This publication makes use of data products from the Wide-field Infrared Survey Explorer, which is a joint project of the University of California, Los Angeles, and the Jet Propulsion Laboratory/California Institute of Technology, funded by the National Aeronautics and Space Administration. This work is based in part on data obtained from the UKIRT Infrared Deep Sky Survey (UKIDSS). CL acknowledges funding through DFG grant LE 3042/1-1. XF acknowledges supports from NSF grants AST 08-06861 and 11-07682. MH is supported by the Nordrhein-Westfälische Akademie der Wissenschaften und der Künste. We thank the anonymous referee for helpful comments on the paper.

Facilities: Herschel, Spitzer.

APPENDIX

APPENDIX MATERIAL

Comments on individual objects

Object names are given in the format *Jhhmm+ddmm*. For full, NED compatible object designations see Table 1.

J0203+0012 ($z = 5.72$). The combined optical and NIR spectroscopy by Mortlock et al. (2009) reveals broad absorption line features in this quasar which could be one explanation for the abrupt change in SED slope observed at $\lambda_{\text{rest}} \lesssim 0.3 \mu\text{m}$ (Fig. 3). It is fairly radio bright at 1.4 GHz compared to most $z \sim 6$ quasar (Wang et al. 2008a) and is detected at 250 GHz with a flux of 1.85 ± 0.46 mJy (Wang et al. 2011). These authors did not detect the quasar in CO(6-5) nor in the corresponding continuum. While clearly seen in all our *Spitzer* observations, no detection was achieved with *Herschel*. Several nearby galaxies can be identified in SDSS and IRAC, some of which are prominent in most infrared channels. The closest bright object is $\sim 30''$ northeast of the quasar. From SDSS spectroscopy of some galaxies in this area it appears that they might belong to a foreground cluster at redshift of $z \sim 0.077$.

J0338+0021 ($z = 5.03$). This source was detected at 250 GHz (3.7 ± 0.3 mJy), but remained undetected at 1.4 GHz (Carilli et al. 2001). The $850 \mu\text{m}$ flux is measured to be 11.9 ± 2.0 mJy (Priddey et al. 2003). Maiolino et al. (2007) report CO(5-4) emission from the quasar, but no continuum at 95.6 GHz is detected. Inspection of the field at optical through FIR wavelengths reveals a nearby source $\sim 15''$ to the west of the quasar. This object is clearly visible in the SDSS *r* and *i* bands, as well as with IRAC and MIPS. In all these filters, the quasar is typically the brighter source, a situation which reverses at 100 and $160 \mu\text{m}$ where the nearby object is ~ 1.4 and ~ 1.3 times brighter, respectively, than the quasar. In all SPIRE bands, however, we only detect a single source. Interestingly, the quasar and the nearby object can both be seen in ground-based $350 \mu\text{m}$ observations (Wang et al. 2008b) and the flux of the quasar (17.7 ± 4.4 mJy/beam) is very comparable to the SPIRE $350 \mu\text{m}$ flux determined for the single detection (18.5 ± 6.0 mJy). This suggests that the SED of the source close to the QSO peaks somewhere around the PACS bands but does not contribute significantly at wavelengths $\gtrsim 350 \mu\text{m}$.

J0756+4104 ($z = 5.11$). The 250 GHz flux (5.5 ± 0.5 mJy) has been presented by Petric et al. (2003) who also detect the source at 1.4 GHz and constrain the size of the radio emission to $< 2.3''$. Priddey et al. (2008) report detections at $850 \mu\text{m}$ (11.2 ± 1.0 mJy) and $450 \mu\text{m}$ (16 ± 5 mJy) where “the source clearly appears elongated” in the $850 \mu\text{m}$ map at a position angle of ~ 70 degrees. We detect the quasar in all our five *Herschel* bands, but the significance is often marginal. Our flux at $350 \mu\text{m}$ is consistent with the ground-based measurements of Wang et al. (2008b).

J0818+1722 ($z = 6.00$). Radio continuum emission at 1.4 GHz is clearly detected (Wang et al. 2007) and the 250 GHz continuum is observed at the 3σ level (1.19 ± 0.38 mJy; Wang et al. 2008a). The close inspection of our

multi-wavelength images reveal a resolved foreground galaxy $\sim 6''$ north-east of the quasar. Both objects, the galaxy and the quasar, are individually detected by MIPS at $24\ \mu\text{m}$ and in shorter wavelength bands. However, only a single source is detected in PACS and SPIRE (note that the spatial resolution of *Herschel*/PACS at $100\ \mu\text{m}$ is comparable to *Spitzer*/MIPS at $24\ \mu\text{m}$). From the relative positions of other sources in the field we can identify the detection at 100, 160, and possibly at $250\ \mu\text{m}$ with the foreground galaxy. It is conceivable that the faint (3.5σ) detection at $350\ \mu\text{m}$ is also due to this source. No detection is achieved at $500\ \mu\text{m}$. In the light of these results, higher resolution mm observation are clearly needed to determine the source of the 250 GHz continuum emission.

J0840+5624 ($z = 5.84$). We do not detect this source in our PACS nor in the SPIRE data. The quasar has been detected at 250 GHz ($3.20 \pm 0.64\ \text{mJy}$), but not at 1.4 GHz (Wang et al. 2007). CO emission is seen in this source (but no continuum at either 85 GHz or 101 GHz) and the $350\ \mu\text{m}$ emission is "marginally detected" from the ground (Wang et al. 2010), which is consistent with our SPIRE $350\ \mu\text{m}$ upper limit. Wang et al. (2010) also report the presence of another source visible at $350\ \mu\text{m}$ as well as at 1.4 GHz located $\sim 30''$ north-west of the quasar. This source is also detected in all our infrared bands. Inspection of the IRAC maps reveals this detection to coincide with two close objects which could be two slightly resolved galaxies separated by $\sim 1.8''$ as seen on an archival *HST*/WFC3 image in the F105W filter.

J0927+2001 ($z = 5.77$). Previously detected at 250 GHz ($4.98 \pm 0.75\ \text{mJy}$; Wang et al. 2007) as well as in CO and in the 90 GHz continuum (Carilli et al. 2007). The $350\ \mu\text{m}$ observations by Wang et al. (2008b) show the quasar ($17.7 \pm 5.7\ \text{mJy beam}^{-1}$) and a secondary source of equal brightness $15''$ to the southeast. While the quasar detection was confirmed in Wang et al. (2010) with better sensitivity ($11.7 \pm 2.4\ \text{mJy beam}^{-1}$), the secondary source was not. We detect the quasar with SPIRE, but not with PACS.

J1044-0125 ($z = 5.78$). This well studied quasar shows a broad CIV absorption feature in its spectrum (e.g. Maiolino et al. 2001; Goodrich et al. 2001). The continuum emission is detected at $850\ \mu\text{m}$ ($5.6 \pm 1.0\ \text{mJy}$; Priddey et al. 2008) and at 250 GHz ($1.82 \pm 0.43\ \text{mJy}$; Wang et al. 2008a). Wang et al. (2010) report the detection of CO (6-5) but can only give an upper limit on the continuum at 102 GHz. The quasar is not seen in ground-based observations at $350\ \mu\text{m}$ (Wang et al. 2010) and 1.4 GHz (Petric et al. 2003). We detect the quasar with PACS, but not with SPIRE.

J1048+4637 ($z = 6.23$). While clearly detected in the available *Spitzer* bands, this quasar remains undetected in our *Herschel* photometry. Wang et al. (2008b) only give an upper limit on the $350\ \mu\text{m}$ flux, just like Robson et al. (2004) at 450 and $850\ \mu\text{m}$. These authors, however note that based on the published 1.2 mm detection ($3.0 \pm 0.4\ \text{mJy}$; Bertoldi et al. 2003), the SCUBA $850\ \mu\text{m}$ observations are deep enough to enable the detection of the source with 4σ significance given a dust temperature of 40 K. At even longer wavelengths, Wang et al. (2010) detect CO(6-5) emission as well as the continuum at 96 GHz. Observations at 1.4 GHz only provide an upper limit on the source flux (Wang et al. 2007).

J1148+5251 ($z = 6.42$). This famous object was the highest redshift quasar known for half a decade (Fan et al. 2003; Willott et al. 2007) and as such has been studied at many wavelengths, including the mm and sub-mm regime. We also have observed this quasar previously with *Herschel*/PACS and reported detections at 100 and $160\ \mu\text{m}$ (Leipski et al. 2010b). Surprisingly, we discovered a secondary object $\sim 10''$ north-west of the quasar which is brighter at $160\ \mu\text{m}$ but can still be identified at $100\ \mu\text{m}$. Ground-based data at $350\ \mu\text{m}$ (Beelen et al. 2006) and 250 GHz (Bertoldi et al. 2003) revealed an intriguing elongation of the quasar detection in the direction of the second source. We argued in our previous paper that this could be an indication for the presence of the secondary source. A possible counterpart is also seen in the $24\ \mu\text{m}$ images. In the IRAC band, three sources are detected around the position of this secondary source, two of which can also be identified on deep *Hubble* Space Telescope (*HST*) images with the ACS camera in the F850LP filter. Recently, new deep *HST* images from WFC3 in the NIR revealed also the third source seen in IRAC. This object is clearly detected, but faint in F125W and gets significantly brighter in F160W. This is our best candidate for a counterpart of the secondary source seen at 24, 100 and $160\ \mu\text{m}$. Surprisingly, however, follow-up observations with the Plateau de Bure Interferometer (PdBI) at 1.2 mm at $\sim 1''$ resolution did not yield a detection and the 3σ upper limit we derive is $0.9\ \text{mJy}$.

Since our initial photometry (Leipski et al. 2010b) we have re-observed the quasar with *Herschel* and obtained new images at 70, 160, 250, 350, and $500\ \mu\text{m}$. While the quasar itself is faintly detected at $70\ \mu\text{m}$, there is no sign for a secondary source. The new $160\ \mu\text{m}$ observations confirm our earlier findings that the flux appears to come from two sources. The source complex is also detected in all SPIRE bands, but the spatial resolution is too low to identify a possible double source. Combining the multi-wavelength photometry of the secondary source, we find that the SED is consistent with a star-forming galaxy at $z \sim 2$ with ULIRG-like luminosity ($L_{8-1000\ \mu\text{m}} \sim \text{few times } 10^{12} L_{\odot}$).

J1335+3533 ($z = 5.90$). The optical spectrum of this source is quite unusual as it shows a typical quasar continuum but virtually no Ly α emission (Fan et al. 2006). At longer wavelengths, the quasar is seen in the *Spitzer* bands, but not in our *Herschel* data. (Wang et al. 2010) report the detection of the CO(6-5) transition and give upper limits on the continuum at $350\ \mu\text{m}$ and 100 GHz. The 250 GHz ($2.34 \pm 0.50\ \text{mJy}$) and 1.4 GHz continuum was detected by Wang et al. (2007).

J2054-0005 ($z = 6.04$). This is the only source in our sample for which we do not have *Spitzer* observations. The SDSS imaging featured a sufficient number of sources that could also be identified on the PACS maps to determine the position of the quasar accurately. The QSO is detected at 250 GHz ($2.38 \pm 0.53\ \text{mJy}$), but not at 1.4 GHz (Wang et al. 2008a). CO observations revealed the (6-5) transition but no continuum at 98 GHz (Wang et al. 2010). We see the source at $160\ \mu\text{m}$ with PACS, but can only give an upper limit on the $100\ \mu\text{m}$ flux. A faint $3-4\sigma$ source is visible at 250 and $350\ \mu\text{m}$. At $500\ \mu\text{m}$ we run into confusion issues with a source located $\sim 30''$ north of the quasar's nominal

position, which can also be identified (separate from the quasars) in the other SPIRE bands and at $160\ \mu\text{m}$. Since our photometry indicates that the FIR peak of the quasar in F_ν falls close to the $250\ \mu\text{m}$ band, we do not expect significant flux in the $500\ \mu\text{m}$ channel. In a NIR spectrum, Ryan-Weber et al. (2009) see a very strong MgII absorber at $z_{\text{abs}} = 2.598$.

REFERENCES

- Barvainis, R. 1987, *ApJ*, 320, 537
- Beelen, A., Cox, P., Benford, D. J., et al. 2006, *ApJ*, 642, 694
- Bertoldi, F., Carilli, C. L., Cox, P., et al. 2003, *A&A*, 406, L55
- Bertoldi, F., Cox, P., Neri, R., et al. 2003, *A&A*, 409, L47
- Carilli, C. L., Bertoldi, F., Rupen, M. P., et al. 2001, *ApJ*, 555, 625
- Carilli, C. L., Neri, R., Wang, R., et al. 2007, *ApJ*, 666, L9
- Cutri, R. M., Wright, E. L., Conrow, T., et al. 2012, Explanatory Supplement to the WISE All-Sky Data Release Products, 1
- Draine, B. T. 2003, *ARA&A*, 41, 241
- Elbaz, D., Dickinson, M., Hwang, H. S., et al. 2011, *A&A*, 533, A119
- Fan, X., Strauss, M. A., Schneider, D. P., et al. 1999, *AJ*, 118, 1
- Fan, X., Narayanan, V. K., Lupton, R. H., et al. 2001, *AJ*, 122, 2833
- Fan, X., Knapp, G. R., Strauss, M. A., et al. 2000, *AJ*, 119, 928
- Fan, X., Strauss, M. A., Schneider, D. P., et al. 2003, *AJ*, 125, 1649
- Fan, X., Hennawi, J. F., Richards, G. T., et al. 2004, *AJ*, 128, 515
- Fan, X., Strauss, M. A., Richards, G. T., et al. 2006, *AJ*, 131, 1203
- Fazio, G. G., Hora, J. L., Allen, L. E., et al. 2004, *ApJS*, 154, 10
- Fruchter, A. S., & Hook, R. N. 2002, *PASP*, 114, 144
- Gallagher, S. C., Richards, G. T., Lacy, M., et al. 2007, *ApJ*, 661, 30
- Goodrich, R. W., Campbell, R., Chaffee, F. H., et al. 2001, *ApJ*, 561, L23
- Griffin, M. J., Abergel, A., Abreu, A., et al. 2010, *A&A*, 518, L3
- Hines, D. C., Backman, D. E., Bouwman, J., et al. 2006, *ApJ*, 638, 1070
- Hönig, S. F., & Kishimoto, M. 2010, *A&A*, 523, A27
- Jiang, L., Fan, X., Hines, D. C., et al. 2006, *AJ*, 132, 2127
- Jiang, L., Fan, X., Annis, J., et al. 2008, *AJ*, 135, 1057
- Jiang, L., Fan, X., Brandt, W. N., et al. 2010, *Nature*, 464, 380
- Kennicutt, R. C., Jr. 1998, *ARA&A*, 36, 189
- Lawrence, A., Warren, S. J., Almaini, O., et al. 2007, *MNRAS*, 379, 1599
- Leipski, C., Meisenheimer, K., Klaas, U., et al. 2010a, *A&A*, 518, L34
- Leipski, C., Haas, M., Willner, S. P., et al. 2010b, *ApJ*, 717, 766
- Lutz, D., Poglitsch, A., Altieri, B., et al. 2011, *A&A*, 532, A90
- Magnelli, B., Lutz, D., Santini, P., et al. 2012, *A&A*, 539, A155
- Maiolino, R., Mannucci, F., Baffa, C., Gennari, S., & Oliva, E. 2001, *A&A*, 372, L5
- Maiolino, R., Neri, R., Beelen, A., et al. 2007, *A&A*, 472, L33
- Markwardt, C. B. 2009, *Astronomical Data Analysis Software and Systems XVIII*, 411, 251
- Mor, R., Netzer, H., & Elitzur, M. 2009, *ApJ*, 705, 298
- Mor, R., & Netzer, H. 2012, *MNRAS*, 420, 526
- Mortlock, D. J., Patel, M., Warren, S. J., et al. 2009, *A&A*, 505, 97
- Nguyen, H. T., Schulz, B., Levenson, L., et al. 2010, *A&A*, 518, L5
- Ott, S. 2010, *Astronomical Data Analysis Software and Systems XIX*, 434, 139
- Pascale, E., Auld, R., Dariush, A., et al. 2011, *MNRAS*, 415, 911
- Petric, A. O., Carilli, C. L., Bertoldi, F., et al. 2003, *AJ*, 126, 15
- Pilbratt, G. L., Riedinger, J. R., Passvogel, T., et al. 2010, *A&A*, 518, L1
- Poglitsch, A., Waelkens, C., Geis, N., et al. 2010, *A&A*, 518, L2
- Popesso, P., Magnelli, B., Buttiglione, S., et al. 2012, arXiv:1211.4257
- Priddey, R. S., & McMahon, R. G. 2001, *MNRAS*, 324, L17
- Priddey, R. S., Isaak, K. G., McMahon, R. G., Robson, E. I., & Pearson, C. P. 2003, *MNRAS*, 344, L74
- Priddey, R. S., Ivison, R. J., & Isaak, K. G. 2008, *MNRAS*, 383, 289
- Richards, G. T., Lacy, M., Storrie-Lombardi, L. J., et al. 2006, *ApJS*, 166, 470
- Rieke, G. H., Young, E. T., Engelbracht, C. W., et al. 2004, *ApJS*, 154, 25
- Robson, I., Priddey, R. S., Isaak, K. G., & McMahon, R. G. 2004, *MNRAS*, 351, L29
- Roseboom, I. G., Oliver, S. J., Kunz, M., et al. 2010, *MNRAS*, 409, 48
- Ryan-Weber, E. V., Pettini, M., Madau, P., & Zych, B. J. 2009, *MNRAS*, 395, 1476
- Savage, R. S., & Oliver, S. 2007, *ApJ*, 661, 1339
- Schlegel, D. J., Finkbeiner, D. P., & Davis, M. 1998, *ApJ*, 500, 525
- Suganuma, M., Yoshii, Y., Kobayashi, Y., et al. 2006, *ApJ*, 639, 46
- Walter, F., Riechers, D., Cox, P., et al. 2009, *Nature*, 457, 699
- Walter, F., Carilli, C., Bertoldi, F., et al. 2004, *ApJ*, 615, L17
- Wang, R., Carilli, C. L., Beelen, A., et al. 2007, *AJ*, 134, 617
- Wang, R., Carilli, C. L., Wagg, J., et al. 2008a, *ApJ*, 687, 848
- Wang, R., Wagg, J., Carilli, C. L., et al. 2008b, *AJ*, 135, 1201
- Wang, R., Carilli, C. L., Neri, R., et al. 2010, *ApJ*, 714, 699
- Wang, R., Wagg, J., Carilli, C. L., et al. 2011, *AJ*, 142, 101
- Werner, M. W., Roellig, T. L., Low, F. J., et al. 2004, *ApJS*, 154, 1
- Willott, C. J., Delorme, P., Omont, A., et al. 2007, *AJ*, 134, 2435
- Wright, E. L., Eisenhardt, P. R. M., Mainzer, A. K., et al. 2010, *AJ*, 140, 1868